



# Properties of Binary Components and Remnant in GW170817 Using Equations of State in Finite Temperature Field Theory Models

Shriya Soma<sup>1,2</sup> and Debades Bandyopadhyay<sup>1,2,3</sup>

<sup>1</sup> Frankfurt Institute for Advanced Studies (FIAS), Ruth-Moufang-Strasse 1, D-60438 Frankfurt am Main, Germany; [soma@fias.uni-frankfurt.de](mailto:soma@fias.uni-frankfurt.de)

<sup>2</sup> Astroparticle Physics and Cosmology Division, Saha Institute of Nuclear Physics (SINP), 1/AF Bidhannagar, Kolkata-700064, India  
[debades.bandyopadhyay@saha.ac.in](mailto:debades.bandyopadhyay@saha.ac.in)

<sup>3</sup> Homi Bhabha National Institute (HBNI), Training School Complex, Anushaktinagar, Mumbai-400094, India

Received 2019 November 19; revised 2020 January 10; accepted 2020 January 10; published 2020 February 21

## Abstract

We investigate gross properties of binary components and remnant in GW170817 using equations of state (EoSs) within the finite temperature field theoretical models. We also adopt finite temperature EoSs in the density-dependent hadron field theory for this study. Properties of binary components are studied using zero temperature EoSs. Particularly, we investigate tidal deformabilities and radii of binary components in light of GW170817. An analytical expression relating the radii and the combined tidal deformability is obtained for binary neutron star masses in the range  $1.1 M_{\odot} \lesssim M \lesssim 1.6 M_{\odot}$ . The upper bound on the tidal deformability gives the upper bound on the neutron star radius as 13 km. Next, the role of finite temperature on the remnant in GW170817 is explored. In this case, we investigate the gravitational and baryon mass, radius, *Kepler* frequency, and moment of inertia of the rigidly rotating remnant for different EoSs at fixed entropy per baryon. The remnant radius is enlarged due to thermal effects compared with the zero temperature case. Consequently, it is found that the *Kepler* frequency is much lower at higher entropy per baryon than that of the case at zero temperature. These findings are consistent with the results found in the literature.

*Unified Astronomy Thesaurus concepts:* Neutron stars (1108); Gravitational waves (678); Astrophysical processes (104)

## 1. Introduction

The discovery of the first pulsar in 1967 by Jocelyn Bell (Hewish et al. 1968) not only led to the quest for the densest form of matter in compact astrophysical objects in this observable universe, but it also prepared the stage to probe the dense matter through gravitational waves when two neutron stars in the binary collided 50 years later on 2017 August 17. This heralded gravitational wave astronomy. The phase evolution of gravitational wave signal in late-stage inspirals encodes the information about the equation of state (EoS) of dense matter through tidal deformation in one neutron star due to the other in a binary neutron star merger. This tidal deformability parameter was extracted for the first time analyzing the gravitational wave signal from the first binary neutron star merger GW170817 and a constraint was imposed on the EoS of dense matter (Abbott et al. 2017a, 2017b, 2018, 2019a).

Neutron stars are unique laboratories for dense matter under extreme astrophysical conditions. After the pulsar discovery, the study of dense matter in terrestrial laboratories gained momentum. Though quantum chromodynamics predicts a very rich phase structure of dense matter, only a small region of it can be probed in laboratories. It has been possible to produce hot and dense matter in heavy ion collisions. Future experimental facilities, such as the International Facility for Antiproton Ion Beam research at GSI, Germany, would create hot (a few tens of MeV) and dense matter (a few times the normal nuclear matter density) relevant for newly born neutron stars. The study of hot and dense matter in laboratories enriches our knowledge of the modification of hadron properties in dense medium, the properties of strange matter involving hyperons, (anti)kaons, and a phase transition from hadrons to quarks. This empirical information from heavy ion collisions is highly valuable in understanding dense matter in

neutron star interior and binary neutron star mergers (Hanauske et al. 2019). This shows that there is a strong interplay between the dense matter produced in heavy ion collisions and formed in neutron star interior.

It is a well-known fact that measured masses, radii, and moments of inertia are the direct probes of dense matter in neutron star interior. Precise mass measurement of pulsars has been possible through the estimation of post-Keplerian parameters, such as Shapiro delay, using pulsar timing. This led to the discoveries of very massive neutron stars (Demorest et al. 2010; Antoniadis et al. 2013). A  $2 M_{\odot}$  neutron star was discovered for the first time employing this technique (Antoniadis et al. 2013). The most massive neutron star is the millisecond pulsar PSR 0740 +6620 with a mass  $2.14^{+0.10}_{-0.09}$  at 68.3% credibility interval which has been reported this year by the North American Nanohertz Observatory for Gravitational Waves (Cromartie et al. 2019). This sets the lower bound on a neutron star's maximum mass. On the other hand, it has been argued that an upper bound on the maximum mass of neutron stars could be placed from electromagnetic observations if the remnant formed in neutron star merger event GW170817 had collapsed to a black hole in a second or so (Margalit & Metzger 2017; Shibata et al. 2017; Rezzolla et al. 2018; Ruiz et al. 2018). The predicted upper bound on the neutron star maximum mass is  $\simeq 2.17 M_{\odot}$ . However, a higher upper bound  $\sim 2.3 M_{\odot}$  has been reported recently (Shibata et al. 2019). Both bounds on the maximum mass of neutron stars put stringent conditions on the composition and EoS of dense matter in neutron star interiors. It has been found that the presence of nonnucleonic forms of matter such as hyperons, kaon condensates, and quarks makes the EoS softer, which might be incompatible with the massive neutron star in most cases.

The radius measurement of neutron stars is a difficult task. The *Neutron Star Composition Explorer* (NICER) mission in

the space station is devoted to the estimation of neutron star radius by observing X-rays from rotation powered pulsars. *NICER* has just published the results on the mass and radius of millisecond pulsar PSR J0030+0451 as  $1.44^{+0.15}_{-0.14} M_{\odot}$  and  $13.02^{+1.24}_{-1.06}$  km (Miller et al. 2019). Riley et al. also reported very similar results of mass ( $1.34^{+0.15}_{-0.16} M_{\odot}$ ) and radius ( $12.71^{+1.14}_{-1.19}$  km) in a different analysis of the *NICER* results (Riley et al. 2019). On the other hand, the extracted value of the combined tidal deformability  $70 \leq \tilde{\Lambda} \leq 720$  from GW170817 provides important information about radii of neutron stars involved in the binary neutron star merger event GW170817 (Abbott et al. 2018; De et al. 2018; Fattoyev et al. 2018; Most et al. 2018; Raithel et al. 2018; Zhao & Lattimer 2018) for the tidal deformability strongly correlates with the radius of a neutron star. All of those calculations indicate that the radius of  $1.4 M_{\odot}$  neutron stars could be  $9 \leq R/\text{km} \leq 14$ .

Valuable information about the EoS of neutron star matter might be imprinted in the postmerger gravitational wave signal from the remnant. The frequency of gravitational waves in the postmerger phase could be as high as a few kilo hertz. LIGO and VIRGO detectors are less sensitive to such high frequencies. Consequently, no postmerger signal was detected from the remnant of GW170817 (Abbott et al. 2019b). Electromagnetic observations provided whatever little information we have about the remnant in GW170817. It was argued that the amount of blue kilonova ejecta as observed in the electromagnetic counterpart of GW170817 might not be compatible with a prompt collapse to a black hole. The fate of the remnant could be one of three possibilities: (i) the delayed collapse of a hypermassive neutron star supported by differential rotation to a black hole in a second or so; (ii) a supramassive neutron star supported by rigid body rotation survives longer before collapsing to a black hole; and (iii) a forever stable neutron star. All three possibilities depend on whether the mass of the remnant is above or below a threshold mass, as well as the maximum mass of the corresponding nonrotating neutron star. It is possible to predict certain properties of the remnant if it becomes a uniformly rotating object. Recently, the LIGO–VIRGO collaboration predicted the moment of inertia and maximum rotation rate of the uniformly rotating remnant at the mass-shedding limit considering a large set of zero temperature EoSs (Abbott et al. 2020).

The binary neutron star merger produces a remnant that is highly hot and dense (Sekiguchi et al. 2011; Endrizzi et al. 2020). This problem has been studied in numerical relativity simulations by different groups (Radice et al. 2017, 2018a; Shibata et al. 2017; Breschi et al. 2019; Cioffi et al. 2019; Most et al. 2019). These simulations predict that the maximum temperature of the remnant could be  $\sim 70$  MeV or more and the maximum density  $\sim 5$  times the normal nuclear matter density. Such high baryon densities in the remnant might lead to the appearance of new degrees of freedom, such as hyperons and quarks (Radice et al. 2017; Most et al. 2019). It also follows from the simulations that the entropy per baryon is  $s_B \lesssim 2k_B$  at the core of the remnant just after the merger whereas the bulk of the remnant outside the unshocked core has the entropy per baryon which is a few times  $k_B$ . Although there is a large spread in temperature and entropy initially, the conditions become homogeneous at a later time. The early evolution of the remnant is driven by gravitational wave radiation over 10–20 ms followed by the later evolution due to viscosity on a timescale of  $\sim 100$  ms and neutrino cooling in 2–3 s (Sekiguchi et al. 2011;

Hotokezaka et al. 2013; Fujibayashi et al. 2018; Kiuchi et al. 2018; Radice et al. 2018a). The magnetic field plays an important role on the evolution of the remnant. An effective viscosity is expected to be generated in the remnant through the magnetorotational instability (MRI). The other effect competing with the MRI is the magnetic winding during differential rotation of the remnant (Hotokezaka et al. 2013). Both effects are responsible for transporting angular momentum and removing the differential rotation making it a rigidly rotating remnant (Cioffi et al. 2019). It would be interesting to investigate the thermal effects on the structures and Keplerian frequencies of a uniformly rotating remnant. The thermal effects on the remnant in BNS merger were earlier studied using EoSs at fixed temperatures (Kaplan et al. 2014). In this work, our motivation is to investigate the properties of the remnant in the numerical library LORENE using EoSs at fixed entropy per baryon (Gourgoulhon et al. 2016).

The paper is organized as follows. In Section 2, different field theory models of EoSs at zero and finite temperatures, as well as the numerical library LORENE for the study of rigidly rotating remnant are described. The results of our calculation are discussed in Section 3. Section 4 contains the summary and conclusions.

## 2. Methodology

We adopt beta-equilibrated and charge neutral EoSs at zero and finite temperatures constructed within the framework of relativistic mean-field (RMF) models with and without density-dependent (DD) couplings to compute tidal deformability, structures of uniformly rotating neutron stars, moment of inertia, and Keplerian frequencies. Baryon–baryon interaction, in RMF models, is mediated by the exchange of  $\sigma$ ,  $\omega$ , and  $\rho$  mesons. Moreover, hyperon–hyperon interaction is mediated by the exchange of  $\phi$  mesons. Furthermore, we consider two classes of EoSs: unified and nonunified. In case of unified EoSs, the same nucleon–nucleon interaction of RMF models is employed in low- and high-density matter. For a nonunified case, we use the RMF model including nonlinear  $\sigma$  meson self-interaction terms to describe the neutron star matter EoS in the core which is matched with the outer and inner crust EoS given by Baym–Pethick–Sutherland and Negele and Vautherin (Baym et al. 1971; Negele & Vautherin 1973).

On the other hand, for unified EoS, an extended version of the nuclear statistical equilibrium (NSE) takes care of the matter made of light and heavy nuclei, and unbound nucleons at low temperatures and below the saturation density (Hempel & Schaffner-Bielich 2010). The interaction among unbound nucleons is dictated by RMF models which are also used to describe the matter at high densities. We exploit different parameterizations of RMF models such as DD2, SFHo, SFHx, TM1, and TMA (Typel et al. 2010; Oertel et al. 2017) for nuclear matter EoS, Banik, Hempel, Bandyopadhyay (BHB)  $\Lambda$  hyperon EoS known as BHB $\Lambda\phi$  EoS (Banik et al. 2014) and hadron-quark (Hybrid) EoS undergoing a first-order phase transition from hadronic to quark matter (Mellinger et al. 2017). We discuss the DD relativistic hadron (DDRH) field theory model at finite temperature along with other unified EoSs in detail in the following paragraphs.

### 2.1. EoS in DDRH Field Theory Model at Finite Temperature

The starting point in this model is the Lagrangian density as given by (Typel et al. 2010; Banik et al. 2014)

$$\begin{aligned}
 L_B = & \sum_{B=n,p,\Lambda} \bar{\Psi}_B (i\gamma_\mu \partial^\mu - m_B + g_{\sigma B} \sigma - g_{\omega B} \gamma_\mu \omega^\mu \\
 & - g_{\rho B} \gamma_\mu \tau_B \cdot \rho^\mu - g_{\phi B} \gamma_\mu \phi^\mu) \Psi_B \\
 & + \frac{1}{2} (\partial_\mu \sigma \partial^\mu \sigma - m_\sigma^2 \sigma^2) - \frac{1}{4} \omega_{\mu\nu} \omega^{\mu\nu} + \frac{1}{2} m_\omega^2 \omega_\mu \omega^\mu \\
 & - \frac{1}{4} \rho_{\mu\nu} \cdot \rho^{\mu\nu} + \frac{1}{2} m_\rho^2 \rho_\mu \cdot \rho^\mu \\
 & - \frac{1}{4} \phi_{\mu\nu} \phi^{\mu\nu} + \frac{1}{2} m_\phi^2 \phi_\mu \phi^\mu.
 \end{aligned} \quad (1)$$

Here,  $m_B$  is the bare baryon mass,  $\tau_B$  is the isospin operator, and  $\Psi_B$  denotes the isospin multiplets for baryons. The parameterization of this model involving only nucleons is known as DD2 (Typel et al. 2010). We extend the Lagrangian to include  $\Lambda$  hyperons and hyperon–hyperon interaction is mediated by  $\phi$  mesons. This model is denoted as BHBA $\phi$  (Banik et al. 2014).

The grand canonical partition function in the mean-field approximation can be written as

$$\begin{aligned}
 \ln Z_B = & \beta V \left[ -\frac{1}{2} m_\sigma^2 \sigma^2 + \frac{1}{2} m_\omega^2 \omega_0^2 + \frac{1}{2} m_\rho^2 \rho_{03}^2 \right. \\
 & \left. + \frac{1}{2} m_\phi^2 \phi_0^2 + \Sigma^r \sum_{B=n,p,\Lambda} n_B \right] \\
 & + 2V \sum_{i=n,p,\Lambda} \int \frac{d^3k}{(2\pi)^3} [\ln(1 + e^{-\beta(E^* - \nu_i)}) \\
 & + \ln(1 + e^{-\beta(E^* + \nu_i)})],
 \end{aligned} \quad (2)$$

where the temperature is defined as  $\beta = 1/T$ ,  $E^* = \sqrt{k^2 + m_B^{*2}}$  and effective baryon mass  $m_B^* = m_B - g_\sigma \sigma$ . The chemical potential of  $i$ th baryon is given by

$$\mu_i = \nu_i + g_{\omega B} \omega_0 + g_{\rho B} \tau_{3B} \rho_{03} + g_{\phi B} \phi_0 + \Sigma^r, \quad (3)$$

and the rearrangement term, which takes care of many-body correlations, has the form

$$\begin{aligned}
 \Sigma^r = & \sum_{B=n,p,\Lambda} \left[ -\frac{\partial g_{\sigma B}}{\partial n_B} \sigma n_B^s + \frac{\partial g_{\omega B}}{\partial n_B} \omega_0 n_B \right. \\
 & \left. + \frac{\partial g_{\rho B}}{\partial n_B} \tau_{3B} \rho_{03} n_B + \frac{\partial g_{\phi B}}{\partial n_B} \phi_0 n_B \right].
 \end{aligned} \quad (4)$$

The total grand canonical partition function of the system is  $Z = Z_B Z_L$ , where  $Z_L$  denotes the grand canonical partition function for noninteracting leptons.

We obtain the equations of motion for meson fields by extremizing  $Z_B$ . Furthermore, we can compute all thermodynamic quantities of baryonic matter using  $Z_B$ . The baryon pressure is written as  $P = TV^{-1} \ln Z_B$  and the energy density of

baryons is

$$\begin{aligned}
 \epsilon = & \frac{1}{2} m_\sigma^2 \sigma^2 + \frac{1}{2} m_\omega^2 \omega_0^2 + \frac{1}{2} m_\rho^2 \rho_{03}^2 + \frac{1}{2} m_\phi^2 \phi_0^2 \\
 & + 2 \sum_{i=n,p,\Lambda} \int \frac{d^3k}{(2\pi)^3} E^* \left( \frac{1}{e^{\beta(E^* - \nu_i)} + 1} + \frac{1}{e^{\beta(E^* + \nu_i)} + 1} \right).
 \end{aligned} \quad (5)$$

The number density of  $i(=n, p, \Lambda)$ th baryon is  $n_i = 2 \int \frac{d^3k}{(2\pi)^3} \left( \frac{1}{e^{\beta(E^* - \nu_i)} + 1} - \frac{1}{e^{\beta(E^* + \nu_i)} + 1} \right)$ . The scalar density for baryon  $B(n_B^s)$  is

$$n_B^s = 2 \int \frac{d^3k}{(2\pi)^3} \frac{m_B^*}{E^*} \left( \frac{1}{e^{\beta(E^* - \nu_B)} + 1} + \frac{1}{e^{\beta(E^* + \nu_B)} + 1} \right). \quad (6)$$

The entropy density of baryons follows from the relation  $S = \beta(\epsilon + P - \sum_{i=n,p,\Lambda} \mu_i n_i)$ , and the entropy density per baryon is  $s = S/n_b$ , where  $n_b$  is the total baryon density.

Nucleon–meson couplings in the DDRH model are DD. The DD2 parameter set of nucleon–meson couplings is used to describe the nuclear matter properties (Typel & Wolter 1999; Typel et al. 2010). The functional forms of DD couplings  $g_{\sigma N}$  and  $g_{\omega N}$  are given by

$$\begin{aligned}
 g_{\alpha N} = & g_{\alpha N}(n_0) f_\alpha(x), \\
 f_\alpha(n_b/n_0) = & a_\alpha \frac{1 + b_\alpha(x + d_\alpha)^2}{1 + c_\alpha(x + d_\alpha)^2},
 \end{aligned} \quad (7)$$

where  $n_0$  is the saturation density;  $\alpha = \sigma$  and  $\omega$ ; and  $x = n_b/n_0$ . For  $\rho$  mesons, we have

$$g_{\rho N} = g_{\rho N}(n_0) \exp[-a_\rho(x - 1)]. \quad (8)$$

Coefficients in both equations, saturation density, nucleon–meson couplings at the saturation density, mass of  $\sigma$  mesons are obtained by fitting the properties of finite nuclei (Typel et al. 2010). The properties of symmetric nuclear matter at the saturation density ( $n_0 = 0.149065 \text{ fm}^{-3}$ ) are consistent with the experimental values (Oertel et al. 2017). The symmetry energy (32.73 MeV) and its density slope (57.94 MeV) are in consonance with experimental findings and observations of neutron stars (Lattimer & Lim 2013; Tews et al. 2017; Lonardon et al. 2019). Furthermore, DD2 EoS is reasonably compatible with that of pure neutron matter obtained in the chiral effective field theory (Oertel et al. 2017; Hebeler et al. 2013).

On the other hand,  $\Lambda$  hyperon–vector meson couplings are determined from the SU(6) symmetry relations (Dover & Gal 1985; Schaffner & Mishustin 1996) and  $\Lambda$  hyperon–scalar meson coupling is extracted from the hypernuclei data. We consider  $\Lambda$  hyperon potential depth  $-30$  MeV in normal nuclear matter (Millener et al. 1988; Schaffner et al. 1992; Mares et al. 1995). Hyperon–meson couplings are taken from Banik et al. (2014). Both DD2 and BHBA $\phi$  EoSs are publicly available from CompOSE and being widely used for supernovae and neutron star merger simulations (Typel et al. 2013).

### 2.2. EoS in Nonlinear Walecka Model at Finite Temperature

Here, we introduce unified Steiner, Fischer, and Hempel EoSs based on NSE model for matter below the saturation density and nonlinear Walecka model with additional meson couplings

(Steiner et al. 2005; Hempel & Schaffner-Bielich 2010). The nonlinear Walecka model with cross meson terms is given by (Steiner et al. 2005)

$$\begin{aligned} \mathcal{L} = & \sum_{B=n,p} \bar{\Psi}_B (i\gamma_\mu \partial^\mu - m_B + g_{\sigma B} \sigma - g_{\omega B} \gamma_\mu \omega^\mu \\ & - \frac{1}{2} g_{\rho B} \gamma_\mu \tau_B \cdot \rho^\mu) \Psi_B + \frac{1}{2} (\partial_\mu \sigma \partial^\mu \sigma - m_\sigma^2 \sigma^2) \\ & - \frac{1}{4} \omega_{\mu\nu} \omega^{\mu\nu} + \frac{1}{2} m_\omega^2 \omega_\mu \omega^\mu \\ & - \frac{1}{4} \rho_{\mu\nu} \cdot \rho^{\mu\nu} + \frac{1}{2} m_\rho^2 \rho_\mu \cdot \rho^\mu - U(\sigma) \\ & + \frac{\kappa}{24} g_{\omega B}^4 (\omega^\mu \omega_\mu)^2 + \frac{\lambda}{24} g_{\rho B}^4 (\rho^\mu \cdot \rho_\mu)^2 \\ & + g_{\rho B}^2 f(\sigma, \omega^\mu \omega_\mu) \rho^\mu \cdot \rho_\mu. \end{aligned} \quad (9)$$

$\tau_B$  is the isospin operator, and  $U(\sigma)$  represents the self-interaction terms, and can be expanded as

$$U(\sigma) = \frac{\zeta}{6} (g_{\sigma B} \sigma)^3 + \frac{\xi}{24} (g_{\sigma B} \sigma)^4, \quad (10)$$

and

$$f(\sigma, \omega^\mu \omega_\mu) = \sum_1^6 a_i \sigma^i + \sum_1^3 b_j (\omega^\mu \omega_\mu)^j. \quad (11)$$

There are 17 parameters in this model. These provide enough freedom to fine tune the low- and high-density part of the isospin sector independently (Steiner et al. 2013). These two EoSs are known as SFHo and SFHx where “o” stands for optimal and “x” stands for extremal. In SFHo, the most probable mass–radius curve of Steiner et al. (2010) was fitted whereas the radius of low-mass neutron stars was minimized in SFHx model resulting in low value (23.18 MeV) for the density slope of the symmetry energy at the saturation density (Steiner et al. 2013). If we neglect last two terms of the Lagrangian density given by Equation (9), it reduces to the same Lagrangian density of TM1 and TMA EoS models with different parameter sets (Sugahara & Toki 1994; Toki et al. 1995). In this case too, a unified EoS was constructed based on the NSE model for the low-density matter and the Lagrangian density without last two terms in Equation (9) for nucleon–nucleon interaction for low as well as high-density matter (Hempel et al. 2012).

### 2.3. Hybrid EoS at Zero Temperature

We also consider an EoS undergoing a first-order phase transition from hadronic to quark matter governed by the Gibbs phase rules. In this case, the hadronic matter is described by the DD2 Lagrangian density of Equation (1) extended to include all hyperons of 1/2-spin baryon octet and  $\Delta$  resonance (Mellinger et al. 2017). The three flavor quark matter is described by the nonlocal extension of the Nambu–Jona-Lasino model as introduced in Mellinger et al. (2017). This hybrid EoS is calculated at temperature  $T = 0$ . This hybrid EoS will be exploited to compute properties of binary components, but not the remnant.

### 2.4. Rapidly Rotating Remnant

Once the differential rotation of the remnant is removed over the effective viscous and magnetic winding timescale  $\sim 100$  ms, the remnant becomes a rigidly rotating body. A stationary, axisymmetric spacetime is assumed for the study of this rigidly rotating remnant formed in GW170817.

Stationary and axisymmetric rapidly rotating star models within general relativity was numerically studied in 3+1 dimensional space plus time framework (Bonazzola et al. 1993). Here, the four-dimensional spacetime manifold is foliated into a family of nonintersecting space-like hypersurfaces  $\Sigma_t$  parametrized by coordinate time,  $t$ . Defining three spatial coordinates ( $x^i$ ) on each hypersurface, one can write the line element in terms of lapse function  $N$  and shift vector ( $\beta^i$ ),

$$ds^2 = -N^2 dt^2 + \gamma_{ij} (dx^i + \beta^i dt) (dx^j + \beta^j dt), \quad (12)$$

where  $\gamma_{ij}$  is the 3 metric on each  $\Sigma_t$ .

Coordinates are chosen for this problem from the consideration of spacetime symmetries and foliation in 3+1 framework. It is assumed here that the spacetime is stationary, axisymmetric, and asymptotically flat. This points to the fact that there are two commuting Killing vector fields ( $\mathbf{e}_0 = \frac{\partial}{\partial t}$  and  $\mathbf{e}_3 = \frac{\partial}{\partial \phi}$ ) in the chosen coordinates ( $x^0 = t$ ,  $x^1 = r$ ,  $x^2 = \theta$ ,  $x^3 = \phi$ ). The remaining two coordinates ( $x^1 = r$ ,  $x^2 = \theta$ ) are chosen as spherical. Furthermore,  $\beta^r = \beta^\theta = 0$ ,  $\gamma_{r\phi} = \gamma_{\theta\phi} = 0$ . Working in a quasi-isotropic gauge, which makes  $\gamma_{r\theta} = 0$ , the line element reduces to the form (Marques et al. 2017)

$$\begin{aligned} ds^2 = & -N^2 dt^2 + A^2 (dr^2 + r^2 d\theta^2) \\ & + B^2 r^2 \sin^2 \theta (d\phi^2 - \beta^\phi dt)^2, \end{aligned} \quad (13)$$

where metric potentials  $N$ ,  $\beta^\phi$ ,  $A$ ,  $B$  depend on coordinates  $r$  and  $\theta$ . Finally, four gravitational field equations were obtained as a set of four coupled elliptic partial differential equations involving energy-momentum tensor in source terms (Bonazzola et al. 1993).

The matter is described by the energy-momentum tensor of a perfect fluid,

$$T^{\mu\nu} = (\varepsilon + P) u^\mu u^\nu + P g^{\mu\nu}. \quad (14)$$

The fluid log-enthalpy is

$$H = \ln \left( \frac{\varepsilon + P}{n m_B} \right), \quad (15)$$

where  $n$  and  $m_B$  are baryon density and rest mass, respectively.

The equation of the fluid equilibrium follows from the conservation of energy-momentum tensor

$$H(r, \theta) + \ln N - \ln \Gamma(r, \theta) = \frac{T e^{-H}}{m_B} \partial_i s - u_\phi u^t \partial_i \Omega, \quad (16)$$

where  $\Gamma$  is the Lorentz factor of the fluid with respect to the Eulerian observer,  $s$  is the entropy per baryon in Boltzmann unit. As we consider only rigid rotation i.e.,  $\Omega = \text{constant}$ , the last term vanishes. It is shown that the equilibrium Equation (16) finally reduces to the zero temperature expression (Marques et al. 2017),

$$H(r, \theta) + \ln N - \ln \Gamma(r, \theta) = \text{const.} \quad (17)$$

We use the numerical library LORENE which implements the above formulation (Gourgoulhon et al. 2016).



**Table 1**

The Saturation Properties of Nuclear Matter Such as Saturation Density ( $n_0$ ), Dimensionless Effective Nucleon Mass, Binding Energy (BE), Incompressibility ( $K$ ), Symmetry Energy ( $S$ ), and Density Slope of Symmetry Energy ( $L$ ) are Obtained Using the Different Parameter Sets

EoS	$n_0$ (fm $^{-3}$ )	$m^*/m$	BE (MeV)	$K$ (MeV)	$S$ (MeV)	$L$ (MeV)	$M_{\text{max}}$ ( $M_{\odot}$ )	$M_B$ ( $M_{\odot}$ )
DD2	0.1491	0.56	16.02	243.0	31.67	55.04	2.42	2.89
BHB $\Lambda\phi$	0.1491	0.56	16.02	243.0	31.67	55.04	2.1	2.43
SFHo	0.1583	0.76	16.19	245.4	31.57	47.10	2.06	2.43
SFHx	0.1602	0.72	16.16	238.8	28.67	23.18	2.13	2.53
TM1	0.1455	0.63	16.31	281.6	36.95	110.99	2.21	2.30
TMA	0.1472	0.64	16.03	318.2	30.66	90.14	2.02	2.30
G230a	0.153	0.78	16.30	230.0	32.50	89.76	2.01	2.31
G230b	0.153	0.70	16.30	230.0	32.50	94.46	2.33	2.75
G240a	0.153	0.78	16.30	240.0	32.50	89.70	2.02	2.75
G240b	0.153	0.70	16.30	240.0	32.50	94.39	2.34	2.75
G300a	0.153	0.78	16.30	300.0	32.50	89.33	2.08	2.40
G300b	0.153	0.70	16.30	300.0	32.50	93.94	2.36	2.78
Hybrid	0.1491	0.56	16.02	243.0	31.67	55.04	2.05	2.39
Exp.	0.15–0.16	0.55–0.75	16.00	220–315	29.00–31.70	45.00–61.90	...	...

**Note.** Maximum mass of nonrotating neutron stars and the corresponding baryon mass are also mentioned here. Experimental values of nuclear matter properties at the saturation density quoted in the last row are taken from Ref. (Stone et al. 2014; Oertel et al. 2017; Hornick et al. 2018; Perego et al. 2019).

### 3. Results and Discussion

We open our discussion with zero temperature EoSs and their role on tidal deformabilities and radii of binary components in GW170817. The saturation properties of various EoSs used here are recorded in Table 1 along the maximum gravitational masses and corresponding baryonic masses. We denote the Walecka model with self-interaction terms of only  $\sigma$  mesons given by Equation (9) as Glendenning (G) followed by incompressibility and a, b for two values of effective masses, i.e., 0.78 and 0.7, respectively. Empirical values of nuclear matter properties are reported in the last row of Table 1. The range of values of incompressibility of nuclear matter at the saturation density is reported in Stone et al. (2014) and Oertel et al. (2017). It was demonstrated that the value of nucleon effective mass  $0.55 \leq m^*/m \leq 0.75$  led to the physical solution for pure neutron matter which was compatible with the chiral effective field theory (Hornick et al. 2018). Tews et al. (2017) reported new bounds on the symmetry energy and its slope. It is evident from the table that the symmetry energy and its slope of several EoS models such as SFHx, TMA, and Glendenning are in tension with experimental values, new bounds of Tews et al., and the state of the art calculations in the chiral effective field theory (Oertel et al. 2017; Tews et al. 2017; Lonardon et al. 2019). The low value of  $L$  in SFHx EoS model was obtained in an attempt to minimize the radii of low-mass neutron stars (Steiner et al. 2013). Figure 1 shows EoSs constructed within the framework of different models as described in Section 2. Two kinks in the hybrid EoS represent the start and end of the mixed phase. The hybrid EoS becomes softer after the mixed phase ends. The low-density part of the SFHx EoS deviates significantly from other EoSs. Furthermore, it is noted that the pressure for SFHx around the saturation density remains constant. This kind of behavior was also noted in the SFHx EoS of pure neutron matter (Fischer et al. 2014). We also plot results of Glendenning EoS models. The mass–radius relationships of these EoSs are exhibited in Figure 2. The gray band indicates the accurately measured pulsar mass of  $2.01 \pm 0.04 M_{\odot}$ . We observe that the lower effective mass leads to higher maximum mass of neutron stars than that of higher values of incompressibility for Glendenning EoS models. Among all

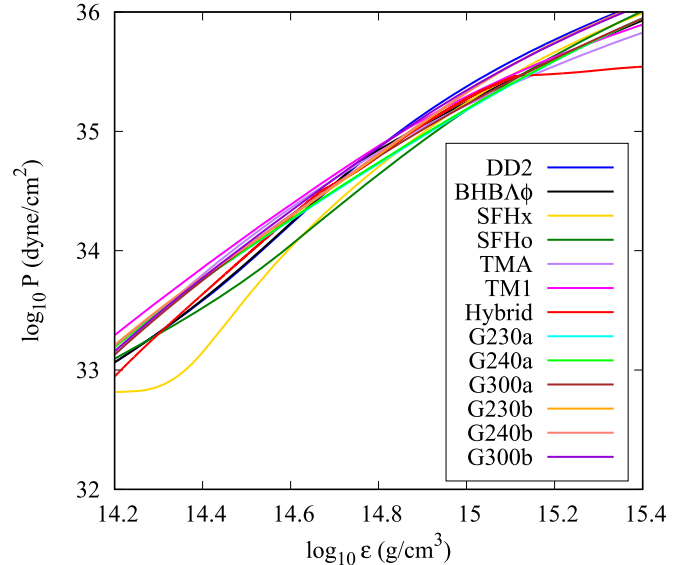


**Figure 1.** Pressure as a function of energy density is plotted for various EoS models at zero temperature.

EoSs, the DD2 EoS results in the highest maximum mass neutron star. Figure 3 shows the plot of dimensionless tidal deformabilities  $\bar{\Lambda}_1$  and  $\bar{\Lambda}_2$  corresponding to binary components with masses  $m_1$  and  $m_2$ , respectively. We apply the same zero temperature EoSs for the calculations of tidal deformabilities. The dotted and dashed lines denote 50% and 90% confidence levels as obtained from the analysis of gravitational wave signal of GW170817 (Abbott et al. 2017a). As one approaches from the top right corner to the bottom left corner, the compactness increases. EoSs predicting less compact neutron stars and lying outside 90% confidence level are ruled out by GW170817, whereas EoSs such as SFHo, SFHx, G230a, and G240a are allowed and BHB $\Lambda\phi$  is marginally allowed. As neutron star masses involved in GW170817 ranged from 1.17 to 1.6  $M_{\odot}$ , the combined tidal deformability probes only a narrow density regime in neutron stars, whereas the maximum mass of a

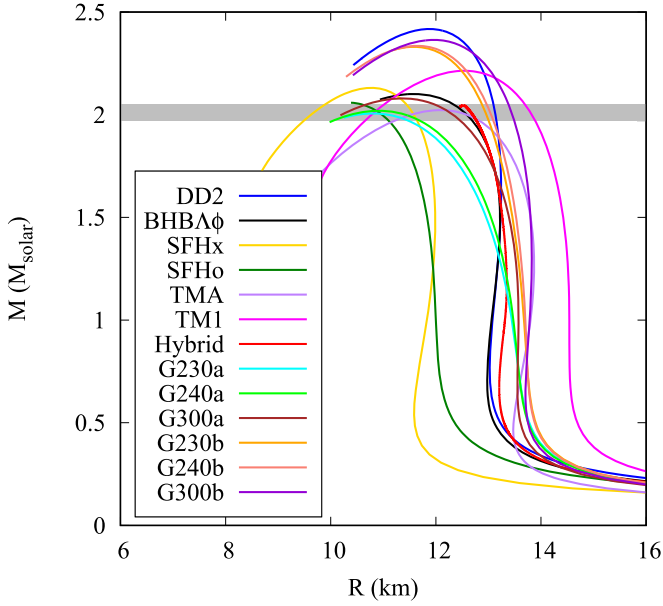


**Figure 2.** Mass–radius relationships are plotted for different EoSs. The gray horizontal band denotes the bound on the neutron star maximum mass.

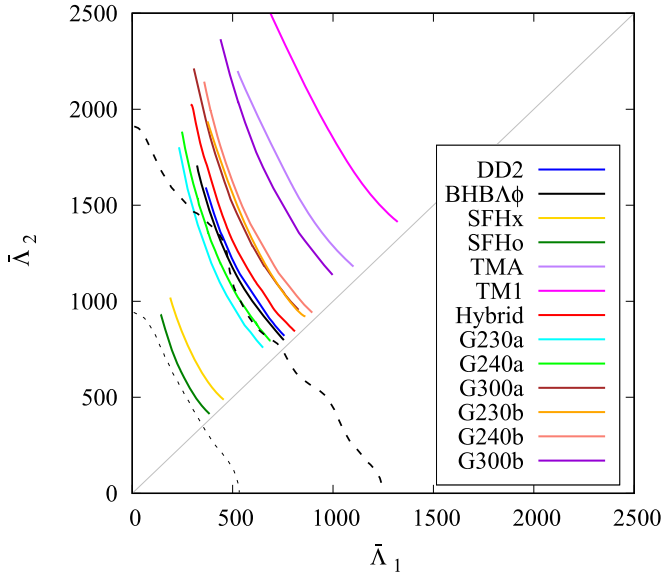


**Figure 3.**  $\bar{\lambda}_1$  is plotted with  $\bar{\lambda}_2$ . Different EoSs are overlaid on this plot. The dotted and dashed lines denote 50% and 90% confidence levels extracted from gravitational wave signal of GW170817.

nonrotating neutron star compatible with the  $2 M_\odot$  pulsar is sensitive to the EoS over a broader range of density from the density of crust to several times the saturation density in the core.

We know that the tidal deformability is closely related to the radius of a neutron star as evident from the expression

$$\bar{\lambda} = \frac{2}{3} k_2 \left( \frac{R}{M} \right)^5. \quad (18)$$

Different groups have already exploited the knowledge of tidal deformability in GW170817 to estimate radii of neutron stars. An analytical approach was prescribed to estimate the radius of a  $1.4 M_\odot$  neutron star relating the value of tidal deformability obtained from GW17017 (Zhao & Lattimer 2018). We extend

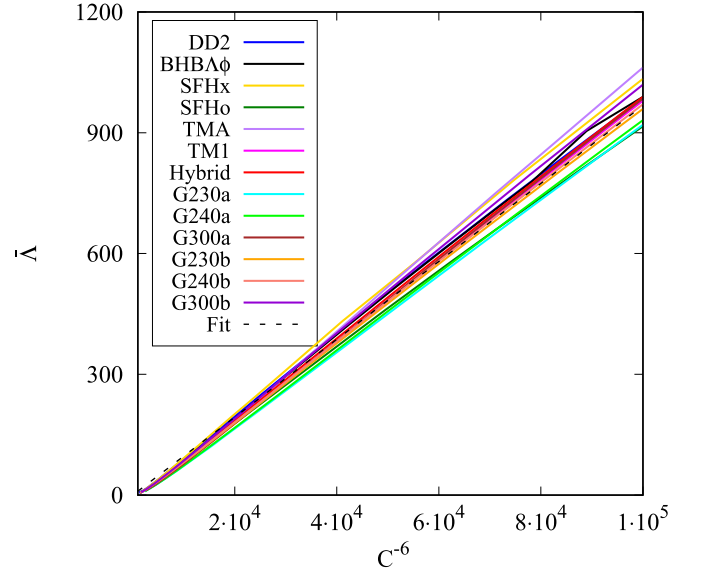


**Figure 4.** Dimensionless tidal deformability is plotted with  $C^{-6}$ , where  $C (= M/R)$  is the compactness.

this prescription to estimate the radius of a neutron star in the mass range  $1.1 M_\odot \lesssim M \lesssim 1.6 M_\odot$ .

It is noted that  $\bar{\lambda} \propto C^{-6}$  because  $k_2 \propto C$ , where  $C = M/R$ , for a large collection of EoSs. We plot this relation in Figure 4 for different EoSs. A fit to the curves with  $\bar{\lambda} = aC^{-6}$  yields the value of  $a \simeq 0.00967$ .

The combined tidal deformability is defined as

$$\tilde{\bar{\lambda}} = \frac{16}{13} \frac{[(m_1 + 12m_2)m_1^4 \bar{\lambda}_1 + (m_2 + 12m_1)m_2^4 \bar{\lambda}_2]}{(m_1 + m_2)^5}, \quad (19)$$

where  $\bar{\lambda}_1$  and  $\bar{\lambda}_2$  are the dimensionless tidal deformabilities of binary neutron star masses  $m_1$  and  $m_2$ , respectively. Using the  $\bar{\lambda} = aC^{-6}$  relation, and assuming radii of neutron stars in the mass range  $1.1 M_\odot \lesssim M \lesssim 1.6 M_\odot$  nearly equal, i.e.,  $R_1 \simeq R_2 \simeq R$ , we get

$$\begin{aligned} \tilde{\bar{\lambda}} &= \frac{16a}{13} \times \frac{1}{(1+q)^5} \\ &\times \left\{ (1+12q) \left( \frac{R}{m_1} \right)^6 + q^4 (q+12) \left( \frac{R}{m_2} \right)^6 \right\} \\ &= \frac{16a}{13} \times \frac{1}{(1+q)^5} \\ &\times \left( \frac{R}{m_1} \right)^6 \left\{ \frac{(1+12q)}{m_1^6} + \frac{(q+12)}{q^2 m_1^6} \right\}. \end{aligned} \quad (20)$$

Writing  $m_1$  in terms of chirp mass by using,  $\mathcal{M} = m_1 q^{3/5} / (1+q)^{1/5}$ ,

$$\tilde{\bar{\lambda}} = \frac{16a}{13} \times \left( \frac{R}{\mathcal{M}} \right)^6 \times \frac{q^{18/5}}{(1+q)^{31/5}} \times [q^2 + 12q^3 + q + 12].$$

Finally, we get

$$\tilde{\bar{\lambda}} = \frac{16a}{13} \times \left( \frac{R}{\mathcal{M}} \right)^6 \times \frac{q^{8/5}}{(1+q)^{26/5}} \times [12 - 11q + 12q^2]. \quad (21)$$

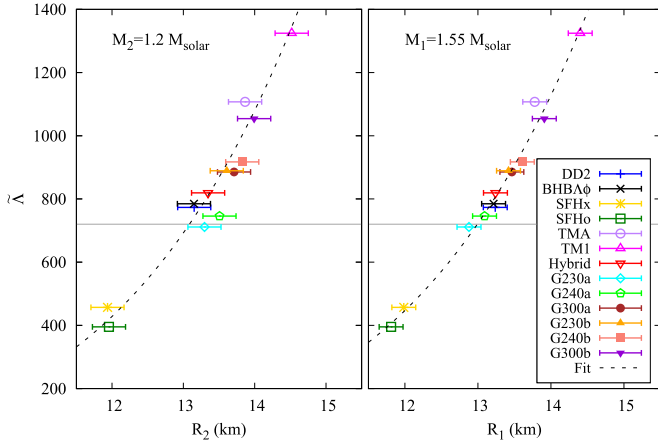


**Figure 5.** Combined tidal deformability  $\tilde{\Lambda}$  is plotted with radius  $R_1$  of primary component mass  $1.55 M_\odot$  in the right panel and radius  $R_2$  of secondary component mass  $1.2 M_\odot$  in the left panel. Symbols with colors represent different EoSs. The horizontal line in both panels is the upper bound on the combined tidal deformability.

It is noted that there is a weak dependence on mass ratio in the combined tidal deformability (Raithel et al. 2018; Radice et al. 2018b; Bhat & Bandyopadhyay 2019). We investigate the extrema of  $\tilde{\Lambda}$  by taking the derivative with respect to  $q$  at a fixed chirp mass and obtain

$$\left( \frac{\partial \tilde{\Lambda}}{\partial q} \right)_{\mathcal{M}} = \tilde{\Lambda} \times \frac{1-q}{5q(1+q)} \times \left[ \frac{96 - 263q + 96q^2}{12 - 11q + 12q^2} \right]. \quad (22)$$

It immediately follows that roots of this derivative are  $q = 1$  and  $q = 0.43346$ . We consider  $m_2^{\min} \sim 1 M_\odot$  and  $m_1^{\max} \sim 2 M_\odot$ , and this implies that the relevant range of  $q$  is clearly  $\geq 0.5$ , whereas for GW170817,  $q \geq 0.7$  (Abbott et al. 2017a). It may be concluded from Equation (21) that the dependence of the combined tidal deformability on chirp mass  $\mathcal{M}$  is similar to that of  $\tilde{\Lambda}$  on  $M$ , i.e.,

$$\tilde{\Lambda} = a' \left( \frac{R}{\mathcal{M}} \right)^6. \quad (23)$$

To find  $a'$ , we can make a substitution of  $q = 0.7$  and  $q = 1$  in Equation (21). This gives  $a' \simeq 0.0042$  for  $q = 1$  and  $a' \simeq 0.0043$  for  $q = 0.7$ . As expected, the value of  $a'$  changes negligibly for the entire relevant range of  $q$  for GW170817.

We can now find the radii of the binary masses which lie in the range  $1.17 - 1.6 M_\odot$  for GW170817 (Abbott et al. 2018).

$$R = 3.669 \times \frac{\mathcal{M}}{M_\odot} \times \tilde{\Lambda}^{1/6}. \quad (24)$$

For the chirp mass  $\mathcal{M} = 1.188$  for GW170817, it becomes

$$R = 4.36 \times \tilde{\Lambda}^{1/6}. \quad (25)$$

If we plug in the upper bound on  $\tilde{\Lambda} = 720$ , we obtain a radius of 13.04 km. Similarly the lower bound of  $\tilde{\Lambda} = 70$  gives a radius of 8.85 km.

It is already known that the tidal deformability is another measure for the radius of a neutron star. We exploit an alternative method to extract the radii of component masses from the upper bound on the combined tidal deformability, set by GW170817. In Figure 5, the combined tidal deformabilities

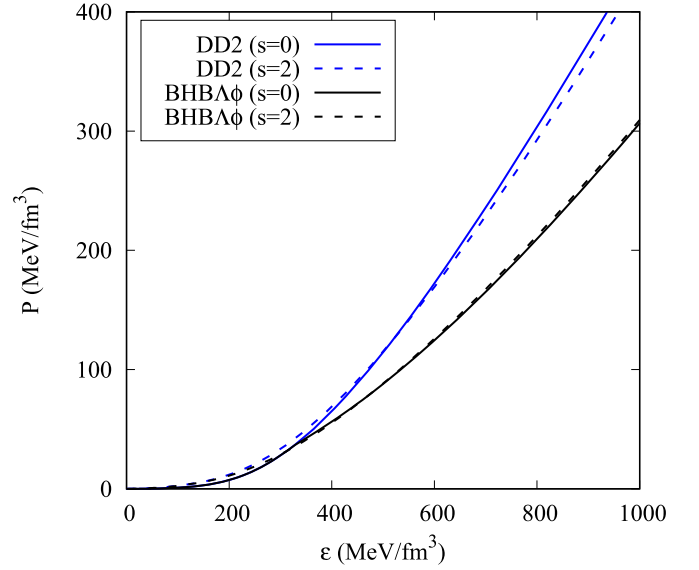


**Figure 6.** Pressure as a function of energy density is plotted for DD2 and BHBA\$\phi\$ EoS models at entropy per baryon  $s = 0$  and  $s = 2$ .

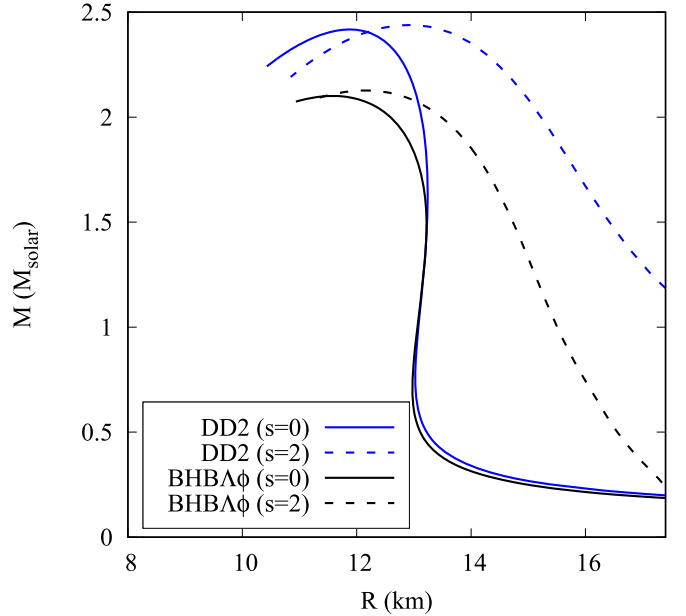


**Figure 7.** Mass-radius relationships are plotted for DD2 and BHBA\$\phi\$ EoSs at entropy per baryon  $s = 0$  and  $s = 2$ .

are plotted as a function of radii corresponding to primary and secondary masses  $1.55$  and  $1.2 M_\odot$  in right and left panels, respectively, for different EoSs as shown in Figure 1. Curves in both panels are fitted with  $\tilde{\Lambda} \propto R^6$ . The error bars are estimated with respect to the fit. The upper bound on the radius of  $1.2 M_\odot$  is 13.08 km, whereas that of  $1.55 M_\odot$  is 12.99 km. These values are in very good agreement with the radius obtained from analytical relation given by Equation (25) using  $\tilde{\Lambda} = 720$ .

Next, we focus on finite temperature EoSs and its impact on the properties of the remnant. We plot the pressure versus energy density and mass-radius relationships of nonrotating neutron star sequences for DD2 and BHBA\$\phi\$ EoSs at entropy per baryon  $s = 0$  and  $s = 2$  in Figures 6 and 7. We find from Figure 7 that the DD2 and BHBA\$\phi\$ EoSs for  $s = 2$  result in

**Table 2**Gravitational Mass of Rigidly Rotating Remnant at the *Kepler* Frequency, the Corresponding Baryon Mass and Moment of Inertia for Entropy/Baryon  $s = 0$ , and  $s = 2$ 

EoS	$s = 0$				$s = 2$			
	$M_G^{\text{Rot}}$ ( $M_\odot$ )	$M_B^{\text{Rot}}$ ( $M_\odot$ )	$I$ ( $10^{38} \text{ kg m}^2$ )	$f_{\text{Kep}}$ (kHz)	$M_G^{\text{Rot}}$ ( $M_\odot$ )	$M_B^{\text{Rot}}$ ( $M_\odot$ )	$I$ ( $10^{38} \text{ kg m}^2$ )	$f_{\text{Kep}}$ (kHz)
DD2	2.606	3.004	5.439	1.236	2.657	2.998	5.400	1.109
BHB $\Lambda\phi$	2.525	2.914	4.204	1.424	2.427	2.717	3.755	1.269
SFHo	2.444	2.856	3.214	1.763	2.447	2.807	3.346	1.606
SFHx	2.556	3.000	4.051	1.581	2.492	2.832	3.715	1.425
TM1	2.623	3.003	5.241	1.228	2.634	3.001	6.767	1.011
TMA	2.439	2.785	4.191	1.315	2.448	2.728	4.460	1.099

higher maximum masses of nonrotating neutron stars due to thermal pressure. However, the thermal effects on the maximum masses are tiny in both cases. Moreover, we observe that radii are much larger for  $s = 2$  than  $s = 0$  case. The thermal effect on the radius is significantly pronounced for DD2 EoS.

Now we explore the thermal effects on the properties of the remnant. Assuming a long lived remnant, the earlier study of maximum rotation rate and moment of inertia of the remnant was carried out by using large numbers of cold and beta-equilibrated EoSs (Abbott et al. 2020). Here, we compute the maximum rotation rate and moment of inertia of the remnant for different finite temperature EoSs using the numerical library LORENE which is best suited for rapidly rotating compact stars at a fixed entropy per baryon. Though the rotation rate of the remnant could exceed the Keplerian limit of the uniformly rotating neutron star having the same baryon mass as the remnant because of differential rotation, the mass-shedding limit was set as the upper limit of the remnant's rotation (Radice et al. 2018a; Abbott et al. 2020). It was estimated in Abbott et al. (2020) that the upper bound of the initial baryon mass of the remnant was  $3.05 M_\odot$ . Some amount of baryon mass ( $< 0.1 M_\odot$ ) was ejected from the remnant. In our analysis, we find that the maximum masses at the Keplerian speed for some EoSs are much higher than  $3.05 M_\odot$ . For those EoSs, we restrict calculations to the baryon mass of  $3 M_\odot$  for the remnant at the mass-shedding limit. We record the baryon mass, moment of inertia, and Keplerian frequencies for EoSs with fixed entropy per baryon  $s = 0$  and  $s = 2$  in Table 2. We find that the Keplerian frequencies at  $s = 2$  for all EoSs are appreciably lower than those of  $s = 0$  cases. We note from our discussion on the thermal effects on radii of neutron stars, as evident in Figure 7, that neutron stars at higher entropy per baryon are bigger in size than that of cold neutron stars. This compensates the increase in mass due to thermal effects keeping the total baryon mass close to that of the cold remnant (Kaplan et al. 2014). The hot remnant attains the mass-shedding limit at significantly lower frequencies than that of the cold remnant. Furthermore, this shows that the Keplerian frequencies of the remnant using zero temperature EoSs are grossly underestimated.

It is worth mentioning here that the thermal effects on the remnant in BNS merger were earlier explored using EoSs at fixed temperatures (Kaplan et al. 2014). This was carried out using a numerical method known as Cook, Shapiro, and Teukolsky solver whereas our calculations are performed in the numerical library LORENE using fixed entropy EoSs. The qualitative outcome of an extended remnant and lower Keplerian frequency due to thermal effects is the same in both

cases. Furthermore, we could impose the constrain on the total baryon mass of the remnant as obtained from the analysis of GW170817 in our calculation.

#### 4. Summary and Conclusions

We have investigated the properties of the binary components and remnant of GW170817 using zero and finite temperature EoSs constructed within the framework of RMF models. The structures and tidal deformabilities of neutron stars involved in the BNS merger are estimated using zero temperature EoSs. All EoSs used in the mass–radius relationship are compatible with the two solar mass neutron star. On the other hand, only soft EoSs and mildly stiff EoSs such as SFHo, SFHx, G230a, G240a, BHB $\Lambda\phi$  are allowed by 50% and 90% confidence intervals on the combined tidal deformability parameter as obtained from the gravitational wave signal of GW170817. It is noted that the tidal deformability in GW170817 and the  $2 M_\odot$  pulsars jointly put strong constraint on the EoS of dense matter. An analytic relation is obtained to estimate the radius of neutron stars involved in the merger using the knowledge of combined tidal deformability. The radius is  $\sim 13$  and  $8.85$  km for the upper and lower bounds on the combined tidal deformability, respectively.

Next the structures, moment of inertia and *Kepler* frequency of the rigidly rotating remnant of GW170817 have been investigated using EoSs at fixed entropy value per baryon  $s = 2$  and compared with those calculated at zero temperature i.e.,  $s = 0$ . We have taken the baryon mass of the remnant  $\lesssim 3 M_\odot$  as estimated in Abbott et al. (2020). Furthermore, the remnant is rigidly rotating at the mass-shedding limit after differential rotation has been eased out due to the effects of viscosity and magnetic winding. It is observed that the thermal effects have very negligible impact on the mass of the remnant. However, the radius of the remnant increases significantly due to the thermal effects compared with the situation at zero temperature. Consequently, we find that the *Kepler* frequency is appreciably lower for  $s = 2$  EoSs than those with  $s = 0$ . It may be concluded that *Kepler* frequency calculated with zero temperature is grossly overestimated in Ref. (The LIGO Scientific Collaboration et al. 2019b).

S.S. acknowledges the support and local hospitality of SINP where a part of this was completed. D.B. acknowledges the fruitful discussion with Horst Stöcker and hospitality at FIAS during this work.

*Software:* LORENE, URL package (Gourgoulhon et al. 2016), CompOSE (Typel et al. 2013), GNU Scientific Library (GSL; Gough 2009).



## ORCID iDs

Shriya Soma  <https://orcid.org/0000-0001-6946-9227>  
 Debades Bandyopadhyay  <https://orcid.org/0000-0003-0616-4367>

## References

- Abbott, B. P., Abbott, R., Abbott, T. D., et al. 2017a, *PhRvL*, **119**, 161101  
 Abbott, B. P., Abbott, R., Abbott, T. D., et al. 2017b, *ApJL*, **848**, L13  
 Abbott, B. P., Abbott, R., Abbott, T. D., et al. 2018, *PhRvL*, **121**, 161101  
 Abbott, B. P., Abbott, R., Abbott, T. D., et al. 2019a, *PhRvX*, **9**, 011001  
 Abbott, B. P., Abbott, R., Abbott, T. D., et al. 2019b, *ApJ*, **875**, 160  
 Abbott, B. P., Abbott, R., Abbott, T. D., et al. 2020, *CQGra*, **37**, 045006  
 Antoniadis, J., Freire, P. C. C., Wex, N., et al. 2013, *Sci*, **340**, 448  
 Banik, S., Hempel, M., & Bandyopadhyay, D. 2014, *ApJS*, **214**, 22  
 Baym, G., Pethick, C. J., & Sutherland, P. 1971, *ApJ*, **170**, 299  
 Bhat, S. A., & Bandyopadhyay, D. 2019, *JPhG*, **46**, 014003  
 Bonazzola, S.,ourgoulhon, E., Salgado, M., & Marck, J.-A. 1993, *A&A*, **278**, 421  
 Breschi, M., Bernuzzi, S., Zappa, F., et al. 2019, *PhRvD*, **100**, 104029  
 Char, P., & Banik, S. 2014, *PhRvC*, **90**, 015801  
 Cioffi, R., Kastaun, W., Kalinani, J. V., & Giacomazzo, B. 2019, *PhRvD*, **100**, 023005  
 Cromartie, H. T., Fonseca, E., Ransom, S. M., et al. 2019, *NatAs*, **4**, 72  
 De, S., Finstad, D., Lattimer, J. M., et al. 2018, *PhRvL*, **121**, 091102  
 Demorest, P. B., Pennucci, T., Ransom, S. M., Roberts, M. S. E., & Hessels, J. W. T. 2010, *Natur*, **467**, 1081  
 Dover, C. B., & Gal, A. 1985, *PrPNP*, **12**, 171  
 Endrizzi, A., Perego, A., Fabbri, F. M., et al. 2020, *EPJA*, **56**, 15  
 Fattoyev, F. J., Piekarewicz, J., & Horowitz, C. J. 2018, *PhRvL*, **120**, 172702  
 Fischer, T., Hempel, M., Sagert, I., Suwa, Y., & Schaffner-Bielich, J. 2014, *EPJA*, **50**, 46  
 Fujibayashi, S., Kiuchi, K., Nishimura, N., Sekiguchi, Y., & Shibata, M. 2018, *ApJ*, **860**, 64  
 Gough, B. 2009, GNU Scientific Library Reference Manual (3rd ed.; Network Theory Ltd.)  
 ourgoulhon, E., Grandclément, P., Marck, J.-A., Novak, J., & Taniguchi, K. 2016, LORENE: Spectral methods differential equations solver, Astrophysics Source Code Library, ascl:1608.018  
 Hanauske, M., Bovard, L., Steinheimer, J., et al. 2019, *JPhCS*, **1271**, 012023  
 Hebeler, K., Lattimer, J. M., Pethick, C. J., & Schwenk, A. 2013, *ApJ*, **773**, 11  
 Hempel, M., Fischer, T., Schaffner-Bielich, J., & Liebendörfer, M. 2012, *ApJ*, **748**, 70  
 Hempel, M., & Schaffner-Bielich, J. 2010, *NuPhA*, **837**, 210  
 Hewish, A., Bell, S. J., Pilkington, J. D. H., et al. 1968, *Natur*, **217**, 709  
 Homick, N., Tolos, L., Zacchi, A., Christian, J.-E., & Schaffner-Bielich, J. 2018, *PhRvC*, **98**, 065804  
 Hotokezaka, K., Kiuchi, K., Kyutoku, K., et al. 2013, *PhRvD*, **88**, 044026  
 Kaplan, J. D., Ott, C. D., O'Connor, E. P., et al. 2014, *ApJ*, **790**, 19  
 Kiuchi, K., Kyutoku, K., Sekiguchi, Y., & Shibata, M. 2018, *PhRvD*, **97**, 124039  
 Lattimer, J. M., & Lim, Y. 2013, *ApJ*, **771**, 51  
 Lonardonì, D., Tews, I., Gandolfi, S., & Carlson, J. 2019, arXiv:1912.09411  
 Mares, J., Friedman, E., Gal, A., & Jennings, B. 1995, *NuPhA*, **594**, 311  
 Margalit, B., & Metzger, B. D. 2017, *ApJL*, **850**, L19  
 Marques, M., Oertel, M., Hempel, M., & Novak, J. 2017, *PhRvC*, **96**, 045806  
 Mellinger, R. D., Jr, Weber, F., Spinella, W., Contrera, G. A., & Orsaria, M. G. 2017, *Univ*, **3**, 1  
 Millener, D. J., Dover, C. B., & Gal, A. 1988, *PhRvC*, **38**, 2700  
 Miller, M. C., Lamb, F. K., Dittmann, A. J., et al. 2019, *ApJL*, **887**, L24  
 Most, E. R., Weih, L. R., Rezzolla, L., & Schaffner-Bielich, J. 2018, *PhRvL*, **120**, 261103  
 Most, E. R., Papenfort, L. J., Dexheimer, V., et al. 2019, *PhRvL*, **122**, 061101  
 Negele, J. W., & Vautherin, D. 1973, *NuPhA*, **207**, 298  
 Oertel, M., Hempel, M., Klähn, T., & Typel, S. 2017, *RvMP*, **89**, 015007  
 Perego, A., Bernuzzi, S., & Radice, D. 2019, *EPJA*, **55**, 124  
 Radice, D., Bernuzzi, S., Del Pozzo, W., Roberts, L. F., & Ott, C. D. 2017, *ApJL*, **842**, L10  
 Radice, D., Perego, A., Bernuzzi, S., & Zhang, B. 2018a, *MNRAS*, **481**, 3670  
 Radice, D., Perego, A., Zappa, F., & Bernuzzi, S. 2018b, *ApJL*, **852**, L29  
 Raithel, C., Özel, F., & Psaltis, D. 2018, *ApJL*, **857**, L23  
 Rezzolla, L., Most, E. R., & Weih, L. R. 2018, *ApJL*, **852**, L25  
 Riley, T. E., Watts, A. L., Bogdanov, S., et al. 2019, *ApJL*, **887**, L21  
 Ruiz, M., Shapiro, S. L., & Tsokaros, A. 2018, *PhRvD*, **97**, 021501  
 Schaffner, J., & Mishustin, I. N. 1996, *PhRvC*, **53**, 1416  
 Schaffner, J., Stöcker, H., & Greiner, C. 1992, *PhRvC*, **46**, 322  
 Sekiguchi, Y., Kiuchi, K., Kyutoku, K., & Shibata, M. 2011, *PhRvL*, **107**, 051102  
 Shibata, M., Fujibayashi, S., Hotokezaka, K., et al. 2017, *PhRvD*, **96**, 123012  
 Shibata, M., Zhou, E., Kiuchi, K., & Fujibayashi, S. 2019, *PhRvD*, **100**, 023015  
 Steiner, A. W., Hempel, M., & Fischer, T. 2013, *ApJ*, **774**, 17  
 Steiner, A. W., Lattimer, J. M., & Brown, E. F. 2010, *ApJ*, **722**, 33  
 Steiner, A. W., Prakash, M., Lattimer, J. M., & Ellis, P. J. 2005, *PhR*, **411**, 325  
 Stone, J. R., Stone, N. J., & Moszkowski, S. A. 2014, *PhRvC*, **89**, 044316  
 Sugahara, Y., & Toki, H. 1994, *NuPhA*, **579**, 557  
 Tews, I., Lattimer, J. M., Ohnishi, A., & Kolometsev, E. E. 2017, *ApJ*, **848**, 105  
 Toki, H., Hiratai, D., Sugahara, Y., Sumiyoshi, K., & Tanihata, I. 1995, *NuPhA*, **588**, c357  
 Typel, S., Oertel, M., & Klähn, T. 2013, arXiv:1307.5715  
 Typel, S., Röpke, G., Klähn, T., Blaschke, D., & Wolter, H. H. 2010, *PhRvC*, **81**, 015803  
 Typel, S., & Wolter, H. H. 1999, *NuPhA*, **656**, 331  
 Zhao, T., & Lattimer, J. M. 2018, *PhRvD*, **98**, 063020